1 Developing A Custom-Built Metal CloudAerosol Processing Chamber: Analysis of Aerosol 2 Coagulation at Low Humidities. 3 Nevil A. Franco, Kyle J. Gorkowski, Katherine B. Benedict 4 Earth and Environmental Science Division, Los Alamos National Laboratory, P.O. Box 1663 5 Los Alamos, NM, US 87545-1663 6 7 Corresponding Authors: 8 9 Kyle J. Gorkowski; gorkowski@lanl.gov 10 Katherine B. Benedict; kbenedict@lanl.gov 11 12 Abstract 13 We are developing have developed an intermediate size (906 L) eloudaerosol processing 14 chamber, and this paper reports on the design and initial characterization of dry aerosol 15 experiments. Specifically, we are determining wall-loss and coagulation correction factors using 16 the observed size distribution measurements for surrogates of common aerosol classes: sodium 17 chloride, sucrose, and soot biomass burning aerosol smoke. Results show that, on average, 18 sodium chloride, sucrose, and sootsmoke wall-loss rates converge to similar values on relatively 19 short time scales (<1 hour). The fitted coagulation correction factor,  $W_c^{-1}$ , for sootsmoke

particles (1.23  $\pm$  0.312), indicates that on average they adhere to each other more than sodium

coagulation correction, but it is consistent with our Monte Carlo error analysis. This study lays

chloride  $(0.969 \pm 0.524)$  and sucrose  $(1.16 \pm 1.38)$ . The relative uncertainty is high for the

20

21

22

**Style Definition:** Bibliography: Indent: Left: 0", First line: 0", Space After: 12 pt, Line spacing: single, Tab stops: Not at 0.18"

Formatted: Font: 12 pt

Formatted: Font: 12 pt

Formatted: Font: Times New Roman

the foundation for future experiments at elevated humidity and supersaturation conditions to characterize the influence of particle shape on coagulation and cloud parameters.

#### 1 Introduction

23

24

25

26

27

28

29

30

31

32

33

34

35

36

37

38

39

40

41

42

43

44

45

Aerosol-cloud interactions remain one of the largest sources of uncertainty in the Earth's radiation budget. By directly scattering, absorbing solar radiation and indirectly influencing cloud formation, acrosols affect longwave and shortwave radiation in the Earth's atmosphere 1. Despite sustained research efforts, these impacts still pose significant challenges to our understanding of the aerosol cooling effect, estimated at  $-0.86 \pm 0.56$  W/m<sup>2</sup>, and the effective anthropogenic radiative forcing of Earth's climate (estimated at -1.25 ± 0.85 W/m<sup>2</sup>)<sup>1</sup>-By directly scattering, absorbing solar radiation and indirectly influencing cloud formation, aerosols affect longwave and shortwave radiation in the Earth's atmosphere (IPCC, 2023). Despite sustained research efforts, these impacts still pose significant challenges to our understanding of the aerosol cooling effect, estimated at  $-0.86 \pm 0.56 \text{ W/m}^2$ , and the effective anthropogenic radiative forcing of Earth's climate (estimated at  $-1.25 \pm 0.85$  W/m<sup>2</sup>)(IPCC, 2023). The complexity of aerosol sources, properties, and processing continues to hinder precise quantification of these forcing estimates. A critical source of aerosols is wildfire smoke, which can influence radiative budgets up to a year depending on the transport and evolution of plumes<sup>2-4</sup>. Under extreme burning conditions, wildfires can generate pyrocumulonimbus clouds, lofting large concentrations of aerosol into the upper troposphere and lower stratosphere<sup>2,5,6</sup>. These smoke particles can exert prolonged effects on climate through chemical and physical processes such as condensation and coagulation<sup>7-9</sup>. The fractal nature of soot particles further complicates our understanding of their indirect effects on cloud formation and radiative properties 10-12. For instance, during the Amazon biomass burning season, Koren et. al. 13 reported a dramatic reduction in cumulus cloud cover from 38% under cleaner conditions to 0% during heavy smoke. However, Kaufman & Koren et. al. 14 observed an increased cloud cover in regions with higher column acrosol concentrations. These discrepancies underscore the complexity of aerosol-cloud interactions, which depend on various factors such as aerosol composition, hygroscopicity, size distribution, supersaturation, and the prevailing atmospheric stability<sup>45</sup>. As wildfires increase in frequency and intensity due to climate change<sup>16</sup>, refining our knowledge of how these aerosols evolve and ultimately affect cloud development is crucial for improving climate models and future predictions. Beyond large-scale aerosol effects, aging aerosols undergo microphysical transformations that can drastically alter their role in cloud processes. Condensation of organics and the mixing of sulfate with black carbon (BC) have both been shown to influence cloud dynamics 17. Recent work indicates that larger BC agglomerates may form preferentially at cloud tops, while the heaviest-coated BC particles are most likely to be seavenged by cloud droplets 18,19. Modeling these highly dynamic processes remains challenging, as it requires accurately representing particle growth, mixing states, and cloud interactions<sup>20-24</sup>. Cloud chambers are valuable research tools for investigating microphysical mechanisms under well-controlled conditions<sup>25-28</sup>. Existing cloud chambers are their own institutional facility in the case of CLOUD at CERN29, AIDA Chamber EUROCHAMP30, and PI chamber at MTU26, All chambers however, come with artifacts - most notably, the loss of particles to chamber walls through gravity, diffusion, convection, and electrostatic forces<sup>31-34</sup>. Previous studies have highlighted the importance of accounting for both size-dependent and time-dependent wall losses<sup>35,36</sup>.

46

47

48

49

50

51

52

53

54

55

56

57

58

59

60

61

62

63

64

65

66

68	In this paper, we introduce the development of a Los Alamos National Laboratory
69	(LANL) cloud chamber, which is specifically designed A critical source of aerosols is wildfire
70	smoke, which can influence radiative budgets up to a year depending on the transport and
71	evolution of plumes (D'Angelo et al., 2022; Guimond et al., 2023; Yu et al., 2019). Under
72	extreme burning conditions, wildfires can generate pyrocumulonimbus clouds, lofting large
73	concentrations of aerosol into the upper troposphere and lower stratosphere (Leach and Gibson,
74	2021; Rodriguez et al., 2020; Yu et al., 2019). These smoke particles can exert prolonged effects
75	on climate through chemical and physical processes such as condensation and coagulation
76	(Fromm et al., 2022; Gorkowski et al., 2024; Reisner et al., 2023). The fractal nature of soot
77	particles further complicates our understanding of their indirect effects on cloud formation and
78	radiative properties (Cotton and Anthes, 2010; Das et al., 2021; June et al., 2022). For instance,
79	during the Amazon biomass burning season, Koren et. al. (2004) reported a dramatic reduction in
80	cumulus cloud cover—from 38% under cleaner conditions to 0% during heavy smoke. However,
81	Kaufman & Koren et. al. (2006) observed an increased cloud cover in regions with higher
82	column aerosol concentrations. These discrepancies underscore the complexity of aerosol-cloud
83	interactions, which depend on various factors such as aerosol composition, hygroscopicity, size
84	distribution, supersaturation, and the prevailing atmospheric stability (Feingold et al., 2001). As
85	wildfires increase in frequency and intensity due to climate change (Cunningham et al., 2024),
86	refining our knowledge of how these aerosols evolve and ultimately affect cloud development is
87	crucial for improving climate models and future predictions.
88	Beyond large-scale aerosol effects, aging aerosols undergo microphysical transformations
89	that can drastically alter their role in cloud processes. Condensation of organics and the mixing
90	of sulfate with black carbon (BC) have both been shown to influence cloud dynamics (Ching et

91	al., 2018). Recent work indicates that larger BC agglomerates may form preferentially at cloud
92	tops, while the heaviest-coated BC particles are most likely to be scavenged by cloud droplets
93	(Taylor et al., 2014; Zanatta et al., 2023). Modeling these highly dynamic processes remains
94	challenging, as it requires accurately representing particle growth, mixing states, and cloud
95	interactions (Ching et al., 2016; Riemer et al., 2009; Yang et al., 2023; Yao et al., 2021; Zaveri et
96	<u>al., 2010).</u>
97	Aerosol chambers are used to understand these chemical and microphysical
98	transformation in controlled conditions (Becker, 2006; Doussin et al., 2023). Many were built for
99	gas-phase and secondary organic aerosol experiments and feature large volumes with Teflon
00	walls to reduce wall losses (Hynes et al., 2005; Shao et al., 2022b). Others are optimized for
01	specific aerosol processes, like bioaerosols (Massabo, 2018). Cloud chambers are a class of
02	chambers for investigating cloud microphysical mechanisms under well-controlled conditions
03	(Chang et al., 2016; Khlystou et al., 1996; Niedermeier et al., 2020; Shao et al., 2022). Existing
04	cloud chambers are their own institutional facility in the case of CLOUD at CERN (The Cloud
05	Collaboration, 2001), AIDA Chamber EUROCHAMP (Wagner et al., 2006), and PI-chamber at
06	MTU (Chang et al., 2016). These types of facilities are critical for advancing science but are
07	often oversubscribed and require significant support to operate.
08	As outlined in many of the papers cited in the previous paragraph, all chambers however,
09	come with artifacts—most notably, the loss of particles to chamber walls through gravity,
10	diffusion, convection, and electrostatic forces (Corner and Pendlebury, 1951; Fotou and Pratsinis,
11	1993; Mahfouz and Donahue, 2020a; Wang et al., 2018). Previous studies have highlighted the
12	importance of accounting for both size-dependent and time-dependent wall losses (Crump et al.,
13	1982; Crump and Seinfeld, 1981).

In this paper, we introduce the development of a Los Alamos National Laboratory

(LANL) aerosol processing chamber, which we use to investigate coagulation processes under simulated conditions. We present initial data from experiments where aerosols were injected in a dry environment to quantify losses to chamber walls, dilution, and coagulation effects. Different types of aerosols were examined to validate known aerosol behaviors and characterize coagulation. We further demonstrate the use of a python based aerosol package, Particula<sup>37</sup>, to model coagulation and wall-loss rates. Through these studies, we aim to refine experimental design and advance understanding of how aerosols—particularly soot—undergo physical transformations that shape their role in cloud formation and climate forcing (Particula, 2025), to model coagulation and wall-loss rates. Through this study, we aim to characterize the behavior of aerosol in the dry chamber (influence of particle composition and shape) and determine conditions suitable for future studies at elevated humidity including supersaturation. In addition, we perform an uncertainty analysis on the coagulation correction retrieval to determine the range of aerosol concentrations that reduce uncertainty in coagulation corrections.

# 2 Chamber Development and Methods

## 2.1 Setup of chamber and experiments

The LANL chamber is in the first phase of development with control of both temperature and humidity to be added in future work. The 906 L\_(0.906 m³, internal volume) chamber is made of 6 stainless steel walls which are inert and reduce the effects of electrostatic charge. The rectangular body and dimensions are shown in Figure 1. The chamber has an internal surface area of 6 m² with surface-to-volume ratio of 6.6 m⁻¹. The chamber's joints are sealed with a fast cure marine adhesive caulk (Sika, Sikaflex 291) and the outside junctions where the walls

intersected were intersect are sealed using ZIP System<sup>TM</sup> Strech Tape (Huber Engineered Woods). Portholes were made for the top and bottom plates where wires and probes be placed for measurements in the chamber and for aerosols to flow in and out of the chamber. Unused portholes are sealed with Swagelok caps and those used for probes and wires are sealed with a rubber gasket or a Teflon ferrule. A leak test was performed by pressurizing the chamber by feeding clean air in and sealing every outlet then seal any leak detected. The chamber is designed to operate at ambient pressure.

Copper tubing lines (3/8") are used to supply aerosols to the chamber and deliver outflow sampling to instrumentation. Zero-air generators (T701 Teledyne Inc., USA) provide clean dry air to push aerosol to the chamber and additional dilution air using Teflon tubing (1/4"). Push flow enters at the bottom of the chamber, creating an upwards direction of flow. Aerosols are sampled from an outlet at the top of the chamber. A dilution flow is connected to the outlet line (88.9 mm from the outlet) to control aerosol concentrations and prevent overwhelming the sampling instruments. A minimum sampling flow rate of 1.5 L/min was needed to supply the instruments and we used a 1:5 ratio of push to dilution for the experiments presented here. This infers a residence timescale within the chamber of 604 minutes (10 hours) and half-life of 418 minutes (6.9 hours). The flow rates are controlled with mass flow controllers (MFC; Alicat). Prior to each experiment the chamber was flushed by pushing clean air with a flow of ~10 L/min for at least 3 hours to reach background (~0-10 cm<sup>-3</sup>).

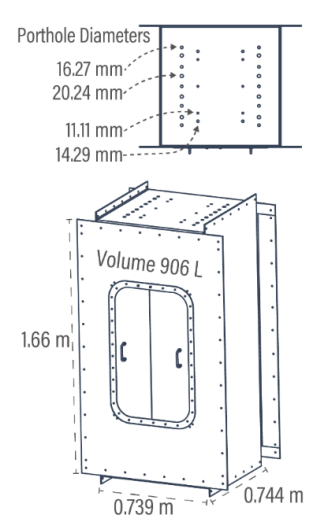


Figure 1. Schematic of LANL's 906 L chamber. The chamber has external dimensions of 1.66 m in height, 0.739 m in width, and 0.744 m in depth. The design includes 56 portholes with diameters ranging from 11.11 mm to 20.24 mm, shown across the top and mirrored on the bottom.

#### 2.2 Aerosol Generation and Instrumentation

Two aqueous solutions and controlled combustion of dried biomaterial were used as the sources of aerosols. Sodium chloride (NaCl; Sigma-Aldrich) was chosen because it is a well-understood compound in aerosol studies. Sucrose (Sigma-Aldrich) was used to act as a secondary organic aerosol surrogate, and it is also a well-studied aerosol. Each were dissolved in deionized water (Milli-Q, 18.2 M $\Omega$ ) in separate solutions and were put on an Atomizer Aerosol Generator (3079, TSI Inc., USA). The particles coming out of the atomizer passed through a silica gel diffusion drier at a generation flow rate of ~2.4 L/min. The duration of aerosol injection varied based on the desired number concentration. To generate sootsmoke, 0.1-0.5 g samples of dried biomaterial *Poa pratensis* (Kentucky bluegrass) were weighed out, placed on a quartz boat and into a quartz-tube furnace (Carbolite Gero, TS1-1200, Verder Scientific, UK)

Formatted: Line spacing: single

Formatted: Font: Bold

that was set to 1000°C for a flaming combustion condition. Soot particles were pushed to the chamber by zero-air at 4 L/min for 5 minutes, an estimated time for This identical setup was used in Benedict et al. (2024) which showed that at 1000°C burn the black carbon mass fraction averaged 17% for biomass fuels with a single scattering albedo of 0.35 (at 523 nm). We expect a similar smoke profile for the experiments presented here thus the smoke injected is a combination of soot, inorganic, and organic mass along with volatile vapors. Smoke particles were pushed to the chamber by zero-air at 4 L/min for 5 minutes, a time window used to ensure complete combustion of the sample. Aerosol size and number distributions downstream of the cloud chamber were measured with a scanning mobility particle sizer (SMPS) that consists of a Differential Mobility Analyzer (3081 DMA, TSI Inc., USA) and a Condensation Particle Counter (3752, TSI Inc., USA). Measurement settings were set to continuously scan for 3 minutes/scan; 160 seconds recording with 20 seconds of purging, measuring sizes 15.7 - 764.5 nm. Our experimental matrix consisted of 5 repeats of NaCl, 4 repeats of sucrose and 6 seetsmoke experiments with varying biomaterial mass, they are outlined in Supplement Information Table 1. In all experiments the first 6 hours of data were used to analyze results.

174

175

176

177

178

179

180

181

182

183

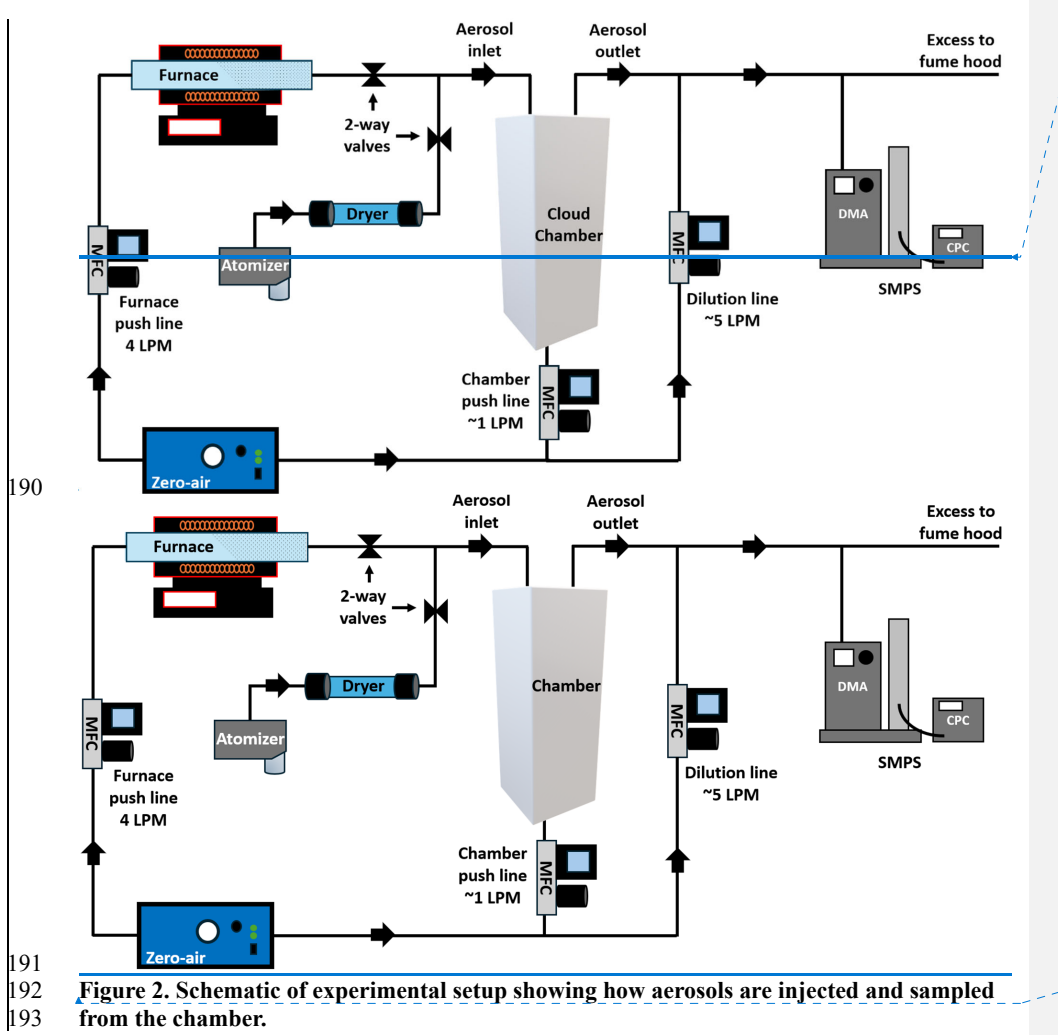
184

185

186

187

188



from the chamber.

194

195

197

# **3 Theory on Chamber Processes**

196 The processing of data from the LANL chamber experiments involved two key steps to analyze

the underlying aerosol processes of coagulation, wall loss, and dilution (chamber push line).

Formatted: Font: Bold

Formatted: Indent: First line: 0", Line spacing: single

Formatted: Indent: First line: 0"

First, we determined the observed size-dependent particle rates:  $dN(D_p)/dt$ . The measured size distributions were fitted to a two-mode lognormal distribution. The lognormal distribution parameters were optimized using the Python library SciPy's optimization routines, with the mean squared error as the cost function. We used multiple minimization methods and selected the best fit for each timestep based on the highest Pearson R-squared value, with a minimum threshold of 0.85. The methods included Nelder-Mead (Simplex algorithm), Powell's method (Powell's conjugate direction method), L-BFGS-B (Limited-memory Broyden-Fletcher-Goldfarb-Shanno with Box constraints), TNC (Truncated Newton Conjugate-Gradient method), SLSQP (Sequential Least Squares Programming), and trust-constr (Trust Region Constrained method). We took this approach since the best fit varied with concentration and shape of the distribution. L-BFGS-B was typically the best for a lognormal distribution, but as the mode became broader (lower concentrations) then TNC, SLSQP or trust-constr would have a higher Pearson R-squared value. The transition of when this would occur was not an obvious concentration threshold. Therefore, we used all optimization routines for each lognormal distribution and selected the best fit based on the highest Pearson R-squared value.

Formatted: Font color: Dark Blue

Second, we fitted these observed rates to theoretical rates calculated from Particula<sup>27</sup>, a python-based aerosol microphysics package. The first step was to generate a new time series at a higher size resolution (log spaced 250 bins), extrapolating to lower (20 nm) and upper (4  $\mu$ m) diameter limits. The size-dependent particle rate was then computed as the linear slope of 21 point moving window (10 before and 10 after). This final rate was subsequently used to fit the underlying aerosol processes in Equation 1 where  $N(D_p)$  represents the number concentration of particles of diameter,  $D_p$ ,  $K_{12}$  is the coagulation kernel,  $W_C^{-1}$  is the coagulation correction factor,

 $N_1$  and  $N_2$  are the concentrations of particles in the bins for  $K_{12}$ ,  $k_{flow}$  is the dilution rate, and  $\beta$ 220 221 is the wall-loss rate. 222 Second, we fitted these observed rates to theoretical rates calculated from Particula 223 (Particula, 2025), a python-based aerosol microphysics package. The first step was to generate a 224 new time series at a higher size resolution (log-spaced 250 bins), starting at 20 nm and 225 extrapolating the 746 nm SMPS upper limit to 4 µm. The size-dependent particle rate was then 226 computed as the linear slope of 21 point moving window (10 before and 10 after). The time 227 window (60 min) was chosen through iteration, as shorter than 20 min had too much noise to 228 have self-consistent results and longer than 90 min had increasing fit residuals. Our 60 min 229 window results in a smoothed time evolution, which Mahfouz and Donahue (2020a) showed to 230 be effective in coagulation analysis. Our moving window approach is different from smog 231 chamber wall-loss experiments where the full 5 hours of the wall-loss experiment would be used 232 to fit an apparent size-dependent, time-invariant wall-loss correction (Wang et al., 2018). 233 The resulting size-dependent rate was subsequently used to fit the underlying aerosol 234 processes in Equation 1 where  $N(D_p)$  represents the number concentration of particles of 235 diameter,  $D_p$ ,  $K_{12}$  is the coagulation kernel,  $W_c^{-1}$  is the coagulation correction factor,  $N_1$  and 236  $N_2$  are the concentrations of particles in the bins for  $K_{12}$ ,  $k_{flow}$  is the chamber flow coefficient, 237 and  $\beta$  is the wall-loss rate.

 $\frac{dN(D_p)}{dt} = W_C^{-1} K_{12} N_1 N_2 - k_{flow} N(Dp) - \beta N(Dp)$  Equation 1

238

239

240

241

The coagulation term is governed by a Brownian Coagulation kernel,  $K_{12}$ , that captures the collision frequency between bin number concentrations ( $N_1$  and  $N_2$ ). This kernel is described in Seinfeld and Pandis<sup>38</sup> (Section 13; Fuchs form with alpha efficiency form of 13.56), (Seinfeld

Formatted: Font: (Intl) Cambria Math

Formatted: Font: (Intl) Cambria Math

Formatted: Font: Times New Roman

242 and Pandis, 2016; Section 13 - Fuchs form with alpha efficiency 13.56), and calculated with
243 Particula. Since  $K_{12}$  does not account for other interactions (e.g. Coulomb interactions) that may
244 lead to coagulation,  $W_C^{-1}$ , the coagulation correction factor, was determined. In our analysis,
245  $W_C^{-1}$  is a free fit parameter to allow for un-modeled behaviors to be represented. The dilution
246 ratechamber flow coefficient,  $k_{flow} = Q/V$ , characterizes how the clean air flow rate (Q) is used
247 to push sample flow out of the chamber volume (V). Finally, the wall-loss term,  $\beta N(Dp)$ ,
248 accounts for the size-dependent removal of particles to the chamber walls.

 $\beta = \frac{1}{LWH} \left( \frac{4H (L+W) \sqrt{k_e D}}{\pi} + v_p LW \times coth \left( \frac{\pi v_p}{4\sqrt{k_e D}} \right) \right)$  Equation 2

Equation 2 shows the wall-loss rate  $(\beta)$  varies with particle size, derived from a rectangular-

250

Formatted: Font: Times New Roman

251 chamber formulation adapted from Crump and Seinfeld<sup>35</sup> and Crump<sup>36</sup>. It incorporates both 252 diffusion-driven transport and gravitational settling. In this formulation, L, W, and H denote the 253 chamber's length, width, and height, respectively; ka is the eddy wall diffusivity (a free fit 254 parameter); D is the particle diffusion coefficient; and  $v_n$  is the particle gravitational settling 255 velocity. 256 257 Equation 2 shows the wall-loss rate  $(\beta)$  varies with particle size, derived from a rectangular-258 chamber formulation adapted from Crump and Seinfeld (1981) and Crump (1982). It 259 incorporates both diffusion-driven transport and gravitational settling. In this formulation, L, W, 260 and H denote the chamber's length, width, and height, respectively; ke is the eddy wall 261 diffusivity (a free fit parameter);  $D_{\underline{i}}$  is the particle diffusion coefficient; and  $v_n$  is the particle 262 gravitational settling velocity. This physics-based wall-loss coefficient is different from Wang et

263	al.'s (2018) method of apparent size-dependent wall-loss fit. In the apparent size-dependent wall-
264	loss fit the rate equation is a two-term first-order rate equation, where there are no physical terms
265	for the size of the chamber or particle settling velocity, in contrast to what we use in Equation 2.
266	The apparent size-dependent wall-loss approach is common for smog chamber experiments
267	(Doussin et al., 2023; Keywood et al., 2004; Loza et al., 2012; Nah et al., 2017; Ng et al., 2007)
268	but would not work here since one of our goals is to specifically determine coagulation. In our
269	case, we need a physics-based wall-loss rate equation, so we can determine if there are any
270	coagulation corrections that could be applied. If we had used the apparent size-dependent wall-
271	loss fit, then there would be little to no residuals for a coagulation correction analysis.
272	3.1 Volume Conservation Analysis
273	If the corrected aerosol volumes remain consistent, within the noise measurement, we can
274	infer that the processes described in Equation 1 accurately represent chamber behavior.
275	Measured volume concentrations in our experiments were corrected by accounting for volume
276	losses due to both wall loss and chamber flow. We calculated the cumulative lost volume and
277	added it back to the measured values at each time point. In smog chamber experiments involving
278	secondary organic aerosol formation, this volume conservation analysis provides a constraint on
279	organic aerosol yields. Supplemental Figure S8 shows an example of our volume conservation
280	plot from a smoke injection experiment. From this analysis, we conclude that volume is
281	conserved and that no measurable condensation of biomass burning organic vapors occurs under
282	our experimental conditions.
283	4 Results and Discussion

4.1 Example Analysis

We show, in Figure 3, the L-BFGS-B optimization routine that was used on Equation 1 for experimental data from the smoke aerosol generated by combusting Kentucky bluegrass. Figure 3a shows the lognormal-fitted size distribution for the entire experiment, where particle growth is evident as the mode diameter shifts to larger sizes over the six-hour period. Figure 3b breaks down the observed rates after 1.5 hours into three calculated, time-varying, size-dependent components: coagulation, dilution, and wall-loss. At that time, coagulation dominates, reducing particles around 100 nm (~0.16 cm<sup>-3</sup> s<sup>-1</sup>) and forming larger particles around 200 nm. From these fits we are specifically interested in the kernel correction factor to better understand the importance of agglomeration of freshly emitted BC fractal-like particles and how it changes in time.



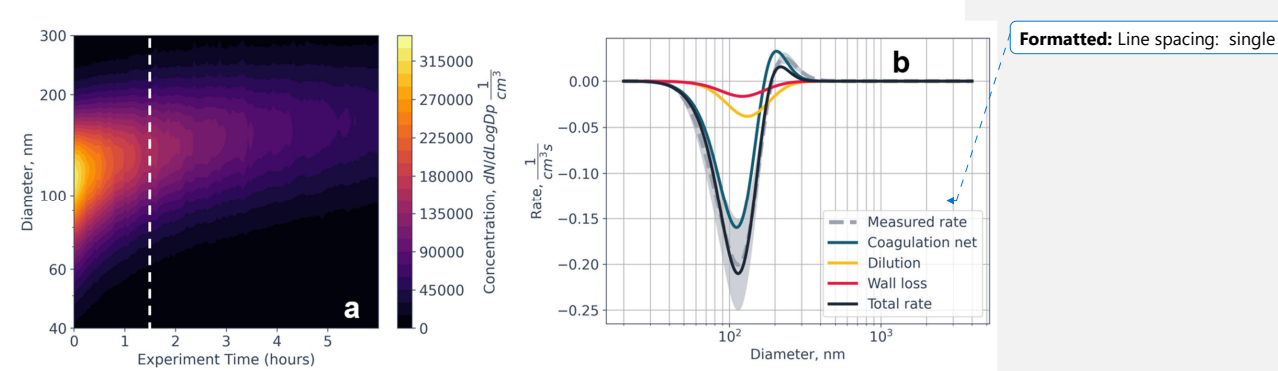


Figure 3. a) Time series of the lognormal-fitted size distribution and concentration for a sootsmoke experiment. The dashed line marks a time slice at approximately 1.5 hours. b) At this time slice, particle loss rates are calculated, revealing both loss and gain of particles due to coagulation. (The time series of rates for individual aerosol species are provided in the Supplement.) Figures S2-S4) In this panel, the dashed gray line represents the measured rate with uncertainty (shaded gray), while the blue, yellow, and pink lines correspond to the coagulation process, dilution, and wall loss, respectively.

Formatted: Font: Bold

## 4.2 Wall-loss Comparison

In Figure 4a we show the average wall-loss rates for our three different aerosol types based on 4-8 experiments each. Only results with valid optimizations and an R-squared above 0.85 were included. In the sucrose experiments, this filter led to data gaps during the later time periods (2-6 hours) for inclusion in the analysis. To better compare with soot, we conducted additional NaCl experiments to have a more complete timeseries for one of the comparisons. The wall loss rates during the first hour (< 1 hour) follow a similar trend apart from NaCl starting at a low wall-loss rate then rising close to a rate of 2 s<sup>-1</sup>. These initial wall-loss rates are consistent with the general observation in chamber studies that early mixing processes and injection conditions can dominate particle loss. Typical ranges reported in smog-chamber experiments span from < 1 s<sup>-1</sup> to tens of s<sup>-1</sup> depending on injection flow and the use of a fan<sup>39</sup>, particle species 40,41, and chamber geometry 40. Over longer times (>1 hours), all three aerosol types converge toward similar wall-loss rates, in agreement with the literature indicating that chamber turbulence and gravitational settling diminish To better compare with smoke, we conducted additional NaCl experiments to have a more complete time series for one of the comparisons. The wall-loss rates during the first hour (< 1 hour) follow a similar trend apart from NaCl starting at a low wall-loss rate then rising close to a rate of 2 s<sup>-1</sup>. These initial wall-loss rates are consistent with the general observation in chamber studies that early mixing processes and injection conditions can dominate particle loss. Typical ranges reported in smog chamber experiments span from < 1 s<sup>-1</sup> to tens of s<sup>-1</sup> depending on injection flow and the use of a fan (Zong et al., 2023), particle species (Li et al., 2017; Wang et al., 2011), and chamber geometry (Wang et al., 2011). Over longer times (>1 hours), all three aerosol types converge toward similar wall-loss rates (0.1 s<sup>-1</sup>), in agreement with the literature indicating that chamber turbulence diminishes over time as mixing subsides.

306

307

308

309

310

311

312

313

314

315

316

317

318

319

320

321

322

323

324

325

326

327

Figure 4b shows the statistical distribution of the wall-loss rates for each aerosol type during the first hour and the subsequent five hours. NaCl and sucrose do not exhibit a large variance in diffusivity for the first hour compared to soot which is 1.12 ± 1.55 s<sup>-1</sup>. NaCl, sucrose, and soot show mean wall-loss rates of 0.562 ± 0.975 s<sup>-1</sup>, 0.233 ± 0.286 s<sup>-1</sup>, and 0.201 ± 0.267 s<sup>-1</sup>, respectively. This convergence to relatively similar values is consistent with past observations in smog-chamber experiments, where turbulent mixing dissipates, and the system approaches a quasi-steady loss rate such as the CMU Teflon chamber <sup>23,34</sup>, the CESAM chamber <sup>40</sup>, and the AIR chamber <sup>26</sup>. However, NaCl and soot sucrose experiments display greater variability than soot, likely due to residual chamber turbulence and differences in particle surface charge stemming from their distinct generation methods (aerosolization vs. combustion).

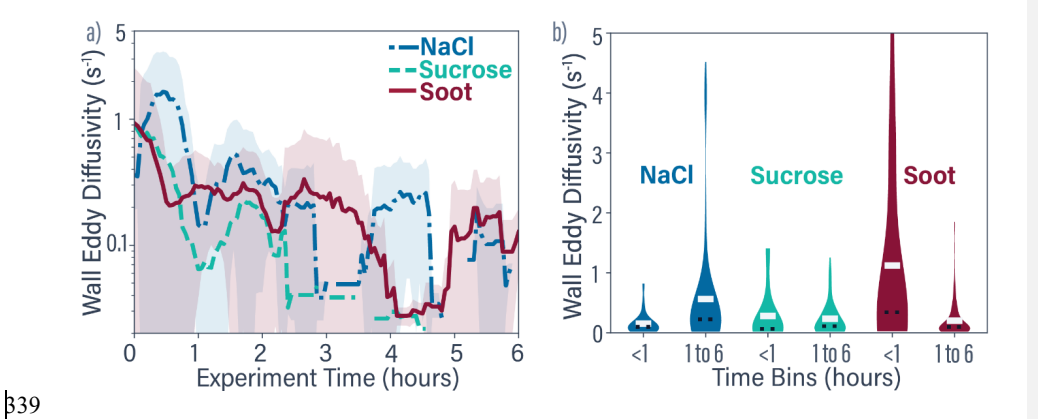


Figure 4b shows the statistical distribution of the wall-loss rates for each aerosol type during the first hour and the subsequent five hours. NaCl and sucrose do not exhibit a large variance in diffusivity for the first hour compared to smoke which is  $1.12 \pm 1.55 \text{ s}^{-1}$ . NaCl, sucrose, and smoke show mean wall-loss rates of  $0.562 \pm 0.975 \text{ s}^{-1}$ ,  $0.233 \pm 0.286 \text{ s}^{-1}$ , and 0.201

± 0.267 s<sup>-1</sup>, respectively. This convergence to relatively similar values is consistent with past observations in smog chamber experiments, where turbulent mixing dissipates, and the system approaches a quasi-steady loss rate such as the CMU Teflon chamber (Mahfouz and Donahue, 2020b; Wang et al., 2018), the CESAM chamber (Wang et al., 2011), and the AIR chamber (Zong et al., 2023). However, NaCl and sucrose experiments display greater variability than smoke, likely due to residual chamber turbulence stemming from their distinct generation methods (aerosolization vs. combustion).

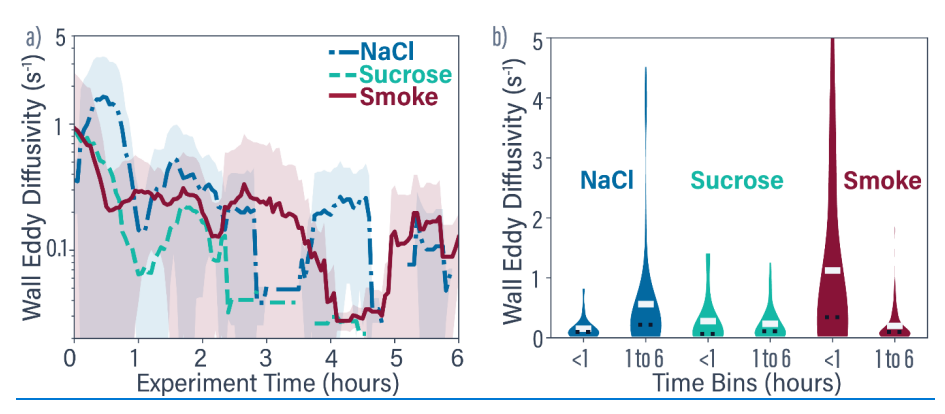


Figure 4. a) Average time series of the calculated wall eddy diffusivity for NaCl (blue), sucrose (green), and seetsmoke (red). Only fits with valid optimizations and r-squared greater than 0.85 are included. b) Violin plots showing the mean (.,), median (white bar) and overall distribution range of wall eddy diffusivity values for each aerosol type in two-time bins (<1 hour and 1–6 hours). The width of each colored region represents the relative density of data points at that value.

# 4.3 Coagulation Corrections

To investigate the influence of interparticle forces on aerosol coagulation, we fitted a coagulation correction factor that would account for van der Waals forces, shape, and/or Coulomb interactions in the coagulation rate. When  $W_C^{-1} = 1$ , collisions are effectively "elastic,"

Formatted: Font: Bold

Formatted: Line spacing: single

Formatted: Font: Bold

Formatted: Font: Bold

with no net enhancement or inhibition. In contrast,  $Wc^{-1} > 1$  indicates that coagulation is enhanced (e.g. due to attractive forces, favorable particle morphology, or turbulence), whereas  $Wc^{-1} < 1$  implies reduced coagulation (e.g. electrostatic repulsion or other inhibiting effects).

In figure 5a., the soot experiments show an initial period where  $W_C^{-1} > 1$ , which may be explained by the fractal nature of soot aggregates that can promote sticking or chain formation upon collision. By the third hour in all experiments, accounting for the variation the average coagulation corrections extend above and below 1. During this later phase, particle concentrations ( $< 3 \times 10^3$  cm<sup>-3</sup>) no longer sustain significant coagulation losses, consistent with prior studies showing that coagulation becomes negligible under low concentration conditions  $^{34,42,43}$ .

In figure 5a., the smoke experiments show an initial period where  $Wc^{-1} > 1$ , which may be explained by the fractal nature of soot aggregates that can promote sticking or chain formation upon collision. By the third hour in all experiments, accounting for the variation the average coagulation corrections extend above and below 1. During this later phase, particle concentrations ( $< 10^4 \, \mathrm{cm}^{-3}$ ) no longer sustain significant coagulation losses, consistent with prior studies showing that coagulation becomes negligible under lower concentration conditions (Hussein et al., 2009; Mahfouz and Donahue, 2020b; Yu et al., 2022).

Figure 5b shows the distribution of coagulation corrections for these time periods. All three aerosols show a mean  $Wc^{-1}$  value around 1 (0.969 ± 0.524 for NaCl, 1.16 ± 1.38 for sucrose, and 1.23 ± 0.312 for sootsmoke), suggesting a slight repulsion or negligible net sticking among particles. However, the standard deviations do encompass  $Wc^{-1} = 1$ . SootSmoke exhibits a slightly higher coagulation corrections initially followed by reduced values (0.941 ± 0.307) in later periods. These observations align with the notion that both particle morphology (e.g., fractal

soot structures) and injection-induced turbulence can transiently enhance coagulation, but the effect diminishes as particles coagulate.

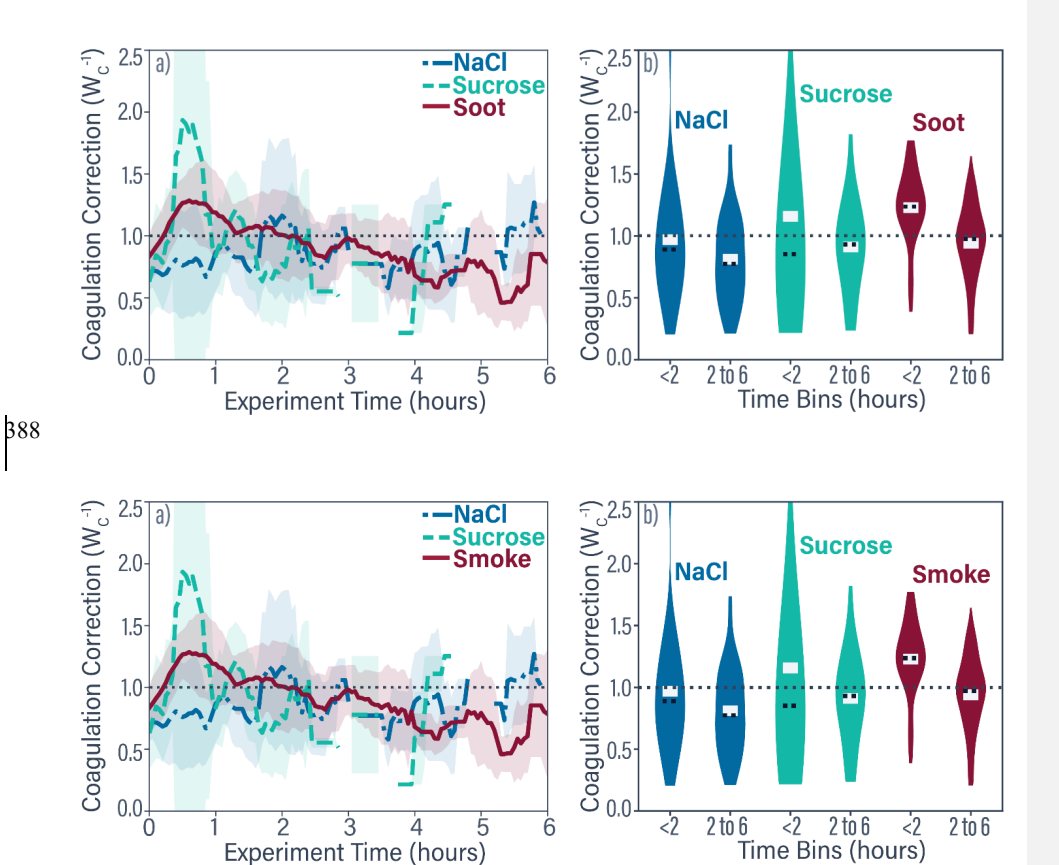


Figure 5. a) Average time series of the calculated coagulation correction for NaCl (blue), sucrose (green), and <a href="seetsmoke">seetsmoke</a> (red). Only fits with valid optimizations and r-squared greater than 0.85 are included. b) Violin plots showing the mean (...), median (white bar) and range of the calculated coagulation correction for each aerosol type averaged across replicate experiments for the indicated time bins (similar to Figure 4b).

Formatted: Font: Bold

Formatted: Line spacing: single

Formatted: Font: Bold

Formatted: Font: Bold

## 4.4 Monte Carlo Error Analysis

To understand the large standard deviations that emerged from our fits of wall loss and coagulation correction, we performed a Monte Carlo error analysis. We began by constructing three number-size distributions, each formed by the sum of two log-normal modes with equal particle numbers. In the first case both modes were centered at 100 nm but differed in geometric standard deviation, i.e., the distribution is summation of a 100 nm mode with a GSD of 1.4 plus a 100 nm mode with a GSD of 1.8. The resulting distribution reflects the broad distributions we observe in our measurements. The second case repeated this structure at 200 nm. The third case was a hypothetical experiment that combined narrow 100 nm and 300 nm modes (both GSD = 1.2) to test the response to a bimodal aerosol distribution.

For every distribution we calculated Equation 1 assuming a wall-eddy diffusivity of 0.1  $s^{-1}$  and a coagulation correction factor ( $Wc^{-1}$ ) of 1.0. This is a null case in which no additional correction to the Brownian coagulation kernel is required. We then superimposed random noise of  $\pm 20\%$  on both the size spectrum and the rate. This noise mirrors uncertainties reported in instrument intercomparisons of  $\pm 10\%$  error between 20 nm and 200 nm and up to  $\pm 30\%$  above 200 nm (Wiedensohler et al., 2012). Thus,  $\pm 20\%$  is a middle point across the range we measured. Applying the same noise to the rate represents the best-case scenario for our analysis pipeline.

With these noisy data sets created, we refit the wall-eddy diffusivity and coagulation correction 80 times at each total number concentration shown in Figure 6. From the ensemble of fits we calculated the percent error in each retrieved parameter and averaged the results (Figure 6). The results in Figure 6 reveal a clear trend percent error. When total number concentration exceeds roughly 10<sup>4</sup> cm<sup>-3</sup>, the uncertainty in the coagulation correction begins to fall. This is

consistent with the fact that Brownian coagulation scales with particle number squared and can be distinguished from measurement noise only at higher concentrations. Conversely, the error in the wall-eddy diffusivity grows with concentration. Once coagulation dominates the particle loss budget, the data contains too little information to constrain the comparatively low wall loss sink, increasing the relative uncertainty. In other words, when coagulation governs the system dynamics, the wall-loss term becomes a minor, poorly resolved correction. The three analyzed distributions exhibit similar percent errors in the coagulation correction. The slightly lower error for the 100 nm mode compared to the 200 nm mode is consistent with the behavior of the Brownian coagulation kernel, where smaller particles have higher coagulation coefficients and therefore undergo more frequent collisions. This leads to a greater rate of change in the distribution for a given number concentration, resulting in better signal-to-noise. The hypothetical bimodal distribution generally shows the lowest uncertainty among the three cases (in our experimental range), although the improvement is modest. Annotations in Figure 6 mark the concentration ranges for the three chamber campaigns, sucrose, NaCl, and smoke aerosols. They also indicate the measured coefficient of variation in the mean coagulation correction for each case. The agreement between these annotated uncertainties and the Monte Carlo error analysis confirms that the observed variability is consistent with the measurement noise.

419

420

421

422

423

424

425

426

427

428

429

430

431

432

433

434

435

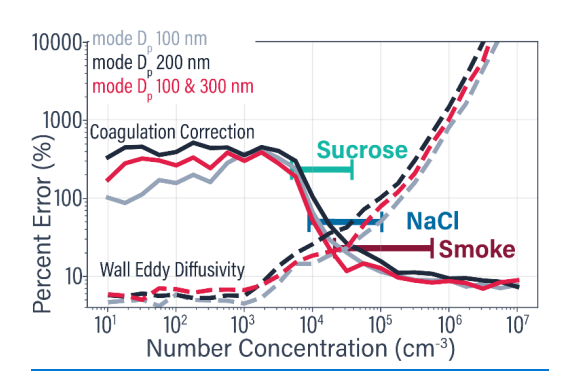


Figure 6: Percent error in fitting of coagulation correction (solid line) and wall eddy diffusivity (dashed line) as a function of number concentration. Lines represent mean errors for size distributions with different modal diameters: 100 nm (gray), 200 nm (black), and a bimodal 100 & 300 nm distribution (red). Annotated markers indicate representative number concentration ranges for Sucrose, NaCl, and Smoke experiments, along with the coefficient of variation (standard deviation divided by the mean) in the coagulation correction, reflecting relative uncertainty rather than bias.

#### 5 Discussion

Our initial experiments in this new-cloud chamber focused on dry conditions and a set of aerosols to quantify how particles evolve in the absence of humidity (<10% relative humidity). Despite the relatively simple setup—no temperature or humidity control—two key insights will be used in future humidified experiments. First, the wall-loss rates converged to similar values across all aerosol types after the first hour, indicating that early differences largely arose from injection flow conditions and subsequent turbulence. Over time, these chamber conditions stabilized, reinforcing the well-documented notion that particle wall losses approach a quasi-steady state as mixing subsides.

A second important finding is that coagulation within the chamber is most pronounced during the initial phase of each experiment. Though this is more uncertain due to larger relative errors. SootSmoke showed signs of coagulation enhancement, potentially attributable to its

fractal structure. Once total number concentrations fell below a few thousand particles per cubic centimeter, coagulation slowed considerably, consistent with the literature. Collectively, these observations highlight the dynamic interplay between wall loss, particle morphology, and injection protocols in shaping the early stages of aerosol evolution in chamber studies.

Our results also shed light on the influence of particle composition and shape. While aerosols like NaCl and sucrose exhibited expected behavior—<u>initialaverage</u> collision enhancements near unity—<u>sootsmoke</u> displayed additional complexity. Early-time coagulation factors for <u>sootsmoke</u> were moderately elevated, suggesting that <u>soot-fractal</u> aggregates <u>within</u> <u>smoke</u> can <u>promote sticking or have an</u> increased collisional radius. Over longer times, the coagulation rates for all three aerosols converged to near unity or below, indicating negligible net enhancement under steady-state conditions. These observations set the stage for more detailed investigations of fractal-like particles under high humidity environments (>90% relative humidity).

Although these initial experiments focused on low humidities, the chamber design allows for temperature and humidity control to be integrated in future work. The Monte Carlo error analysis points to using number concentrations above 10<sup>6</sup> cm<sup>-3</sup> for reducing the percent error in future coagulation correction experiments. Extending to more complex atmospherically relevant aerosol mixtures—such as sootsmoke mixed with organic vapors or inorganic salts—will further elucidate aerosol aging pathways and eloudcoagulation interactions. Additionally, the use of more advanced aerosol instrumentation will improve the characterization of particle morphologies and mixing states that evolve during cloud processing.

#### 6 Conclusion

The custom-built 906 L stainless-steel chamber provided reproducible measurements of particle size distributions under dry conditions, confirming its suitability for controlled aerosol research. Although initial turbulence drove high wall-loss rates, these converged to stable values across NaCl, sucrose, and soot—underscoringsmoke. This underscores that injection protocols and mixing strongly influence early aerosol behavior. The chamber's intermediate size and flexible design for future temperature and humidity controls make it a useful platform to investigate aerosol-cloud interactions more comprehensively. Integrating additional measurements of particle shape, chemical composition, and mixing state will further clarify the complexities of aerosol aging and cloud formation. Building on these dry experiments, upcoming work at higher humidity will reveal how aerosol coagulation and phase changes affect cloud processes such as droplet activation and scavenging. By disentangling coagulation, dilution, and wall-loss mechanisms, this chamber ultimately enables rigorous study of aerosol transformations—, particularly for fractal soot—smoke, in cloud-relevant environments, helping advance both scientific understanding and climate prediction.

Author contributions. NAF performed the experiments, contributed to the analysis of the results, and wrote the manuscript. KJG was responsible for the design of the chamber and the study, development of the data analysis methods, and contributed to the writing of the manuscript. KBB contributed to the design of the study, analysis of the results, and contributed to the writing of the manuscript.

Competing interests. The authors declare no competing interests.

Formatted: Indent: First line: 0.5"

502		
503	Code/Data availability. The python data analysis code is available from corresponding authors.	
504		
505	Acknowledgments. The authors would like to thank Hannah Brink, Ryan Farley, James E. Lee,	
506	and Matt Nelson for their feedback on the manuscript. Release Number LA-UR-25-22994.	
507		
508	Financial support. Research presented in this article was supported by the Laboratory Directed	
509	Research and Development program of Los Alamos National Laboratory under project number	
510	20230248ER. This work was supported by the U.S. Department of Energy through the Los	
511	Alamos National Laboratory. Los Alamos National Laboratory is operated by Triad National	
512	Security, LLC, for the National Nuclear Security Administration of U.S. Department of Energy	
513	(Contract No. 89233218CNA000001).	
514		
515	References	Formatted
516 517	1. Intergovernmental Panel On Climate Change (Ipcc). Climate Change 2021 – The Physical Science Basis: Working Group I Contribution to the Sixth Assessment Report of the	
518	Intergovernmental Panel on Climate Change. (Cambridge University Press, 2023). doi:10.1017/9781009157896.	
519		
520 521	2. Yu, P. et al. Black carbon lofts wildfire smoke high into the stratosphere to form a persistent plume. Science <b>365</b> , 587–590 (2019).	
522	3. Particula: https://uncscode.github.io/particula/, last access: 21 July 2025.	
523 524	Benedict, Katherine. B., Lee, J. E., Kumar, N., Badal, P. S., Barbato, M., Dubey, M. K., and Aiken, A. C.: Wildland Urban Interface (WUI) Emissions: Laboratory Measurement of Aerosol	
525 526	and Trace Gas from Combustion of Manufactured Building Materials, ACS EST Air, https://doi.org/10.1021/acsestair.4c00217, 2024.	
527	Chang, K., Bench, J., Brege, M., Cantrell, W., Chandrakar, K., Ciochetto, D., Mazzoleni, C.,	
528	Mazzoleni I. R. Niedermeier D. and Shaw R. A.: A Laboratory Facility to Study Gas-	

529 530 531	Aerosol–Cloud Interactions in a Turbulent Environment: The Π Chamber, Bulletin of the American Meteorological Society, 97, 2343–2358, https://doi.org/10.1175/BAMS-D-15-00203.1, 2016.
532 533 534	Ching, J., Riemer, N., and West, M.: Black carbon mixing state impacts on cloud microphysical properties: Effects of aerosol plume and environmental conditions, JGR Atmospheres, 121, 5990–6013, https://doi.org/10.1002/2016JD024851, 2016.
535 536 537	Ching, J., West, M., and Riemer, N.: Quantifying Impacts of Aerosol Mixing State on Nucleation-Scavenging of Black Carbon Aerosol Particles, Atmosphere, 9, 17, https://doi.org/10.3390/atmos9010017, 2018.
538 539 540	Corner, J. and Pendlebury, E. D.: The Coagulation and Deposition of a Stirred Aerosol, Proceedings of the Physical Society. Section B, 64, 645–654, https://doi.org/10.1088/0370-1301/64/8/304, 1951.
541 542	Cotton, W. R. and Anthes, R. A.: Storm and cloud dynamics, Academic Press, San Diego, 883 pp., 2010.
543 544 545	Crump, J. G. and Seinfeld, J. H.: Turbulent deposition and gravitational sedimentation of an aerosol in a vessel of arbitrary shape, Journal of Aerosol Science, 12, 405–415, https://doi.org/10.1016/0021-8502(81)90036-7, 1981.
546 547	Crump, J. G., Flagan, R. C., and Seinfeld, J. H.: Particle Wall Loss Rates in Vessels, Aerosol Science and Technology, 2, 303–309, https://doi.org/10.1080/02786828308958636, 1982.
548 549 550	Cunningham, C. X., Williamson, G. J., and Bowman, D. M. J. S.: Increasing frequency and intensity of the most extreme wildfires on Earth, Nat Ecol Evol, 8, 1420–1425, https://doi.org/10.1038/s41559-024-02452-2, 2024.
551 552 553 554	D'Angelo, G., Guimond, S., Reisner, J., Peterson, D. A. &., and Dubey, M.: Contrasting Stratospheric Smoke Mass and Lifetime From 2017 Canadian and 2019/2020 Australian Megafires: Global Simulations and Satellite Observations. JGR Atmospheres, 127, e2021JD036249-(, https://doi.org/10.1029/2021JD036249, 2022).

Guimond, S. R., Reisner, J. & Dubey, M. The Dynamics of Megafire Smoke Plumes in

Rodriguez, B., Lareau, N. P., Kingsmill, D. E. & Clements, C. B. Extreme Pyroconvective

Leach, R. N. & Gibson, C. V. Assessing the Potential for Pyroconvection and Wildfire Blow

Climate Models: Why a Converged Solution Matters for Physical Interpretations. J Adv Model

Updrafts During a Megafire. Geophysical Research Letters 47, e2020GL089001 (2020).

Ups. J. Operational Meteor. 47–61 (2021) doi:10.15191/nwajom.2021.0904.

555

556

557

558

559

560

561

Earth Syst 15, e2022MS003432 (2023).

Formatted: Font: Times New Roman

Formatted: Font: Times New Roman

Formatted: Font: Times New Roman

Formatted: Font: Times New Roman, Not Italic

Formatted: Font: Times New Roman, Not Bold

Formatted: Font: Times New Roman, Not Bold

Formatted: Font: Times New Roman

562	7. Fromm, M., Servranckx, R., Stocks, B. J. & Peterson, D. A. Understanding the critical	
563	elements of the pyrocumulonimbus storm sparked by high-intensity wildland fire. Commun	
564	Earth Environ 3, 243 (2022).	
565	8. Reisner, J. M. et al. Informed Multi-Scale Approach Applied to the British Columbia Fires	
566	of Late Summer 2017. JGR Atmospheres 128, e2022JD037238 (2023).	
500	01 Eace 341111161 2017.3017161103p116163 <del>220</del> , 6202230037230 (2023).	
567	9. Gorkowski, K. et al. Insights into Pyrocumulus aerosol composition: black carbon content	
568	and organic vapor condensation. Environ. Sci.: Atmos. 4, 80–87 (2024).	
569	10. Cotton, W. R. & Anthes, R. A. Storm and Cloud Dynamics. (Academic Press, San Diego,	
570	<del>2010).</del>	
571	11. Das, S., Colarco, P. R., Oman, L. D., Taha, G. &., and Torres, O.,.: The long-term	
572	transport and radiative impacts of the 2017 British Columbia pyrocumulonimbus smoke aerosols	
573	in the stratosphere. Atmos. Chem. Phys. 21, 12069–12090 4, https://doi.org/10.5194/acp-21-	
574	12069-2021)-, 2021.	
[		
575	12. June, N. A. et al. Doussin, JF., Fuchs, H., Kiendler-Scharr, A., Seakins, P., and Wenger,	
576	J. (Eds.): A Practical Guide to Atmospheric Simulation Chambers, Springer International	
577	Publishing, Cham, https://doi.org/10.1007/978-3-031-22277-1, 2023.	
578	Feingold, G., Remer, L. A., Ramaprasad, J., and Kaufman, Y. J.: Analysis of smoke impact on	
579	clouds in Brazilian biomass burning regions: An extension of Twomey's approach, J. Geophys.	
580	Res., 106, 22907–22922, https://doi.org/10.1029/2001JD000732, 2001.	
581	Fotou, G. P. and Pratsinis, S. E.: A Correlation for Particle Wall Losses by Diffusion in Dilution	
582	Chambers, Aerosol Science and Technology, 18, 213–218,	
583	https://doi.org/10.1080/02786829308959596, 1993.	
584	Fromm, M., Servranckx, R., Stocks, B. J., and Peterson, D. A.: Understanding the critical	
585	elements of the pyrocumulonimbus storm sparked by high-intensity wildland fire, Commun	
586	Earth Environ, 3, 243, https://doi.org/10.1038/s43247-022-00566-8, 2022.	
587	Gorkowski, K., Koo, E., Jordan, S., Reisner, J., Benedict, K. B., and Dubey, M.: Insights into	
588 589	Pyrocumulus aerosol composition: black carbon content and organic vapor condensation, Environ. Sci.: Atmos., 4, 80–87, https://doi.org/10.1039/D3EA00130J, 2024.	
569	Environ. Sci., Atmos., 4, 60–67, https://doi.org/10.1059/D5EA001503, 2024.	
590	Guimond, S. R., Reisner, J., and Dubey, M.: The Dynamics of Megafire Smoke Plumes in	
591	Climate Models: Why a Converged Solution Matters for Physical Interpretations, J Adv Model	
592	Earth Syst, 15, e2022MS003432, https://doi.org/10.1029/2022MS003432, 2023.	
502	Harris T Harris A Dahlamani D Drambani I Harris I IV 1 1 M 1	
593 594	Hussein, T., Hruška, A., Dohányosová, P., Džumbová, L., Hemerka, J., Kulmala, M., and Smolík, J.: Deposition rates on smooth surfaces and coagulation of aerosol particles inside a test	
594 595	chamber, Atmospheric Environment, 43, 905–914,	
596	https://doi.org/10.1016/j.atmosenv.2008.10.059, 2009.	
570	maps. Activity 1011010 Junitodelly 2000.101027, 2002.	

Formatted: Font: Times New Roman Formatted: Font: Times New Roman, Not Italic Formatted: Font: Times New Roman Formatted: Font: Times New Roman, Not Bold Formatted: Font: Times New Roman Formatted: Font: Times New Roman Formatted: Font: Times New Roman

- 597 IPCC: Climate Change 2021 The Physical Science Basis: Working Group I Contribution to the
- 598 Sixth Assessment Report of the Intergovernmental Panel on Climate Change, Cambridge
- University Press, Cambridge, https://doi.org/10.1017/9781009157896, 2023.
- June, N. A., Hodshire, A. L., Wiggins, E. B., Winstead, E. L., Robinson, C. E., Thornhill, K. L.,
- 601 Sanchez, K. J., Moore, R. H., Pagonis, D., Guo, H., Campuzano-Jost, P., Jimenez, J. L., Coggon,
- M. M., Dean-Day, J. M., Bui, T. P., Peischl, J., Yokelson, R. J., Alvarado, M. J., Kreidenweis, S.
- 603 M., Jathar, S. H., and Pierce, J. R.; Aerosol size distribution changes in FIREX-AQ biomass
- burning plumes: the impact of plume concentration on coagulation and OA
- condensation/evaporation-Atmos. Chem. Phys-22, 12803–12825-
- 606 https://doi.org/10.5194/acp-22-12803-2022}-, 2022.
- 607 13. Kaufman, Y. J. and Koren, I.: Smoke and Pollution Aerosol Effect on Cloud Cover,
- 608 Science, 313, 655–658, https://doi.org/10.1126/science.1126232, 2006.
- 609 Keywood, M. D., Varutbangkul, V., Bahreini, R., Flagan, R. C., and Seinfeld, J. H.: Secondary
- 610 Organic Aerosol Formation from the Ozonolysis of Cycloalkenes and Related Compounds,
- Environ. Sci. Technol., 38, 4157–4164, https://doi.org/10.1021/es0353630, 2004.
- Khlystou, A., Kos, G. P. A., and Ten Brink, H. M.: A High-Flow Turbulent Cloud Chamber,
- 613 Aerosol Science and Technology, 24, 59–68, https://doi.org/10.1080/02786829608965352, 1996.
- Koren, I., Kaufman, Y. J., Remer, L. A. and Martins, J. V. Measurement of the Effect of
- Amazon Smoke on Inhibition of Cloud Formation, Science, 303, 1342–1345-(2004),
- https://doi.org/10.1126/science.1089424, 2004,
- 617 14. Kaufman, Y. J. & Koren, I. Smoke and Pollution Aerosol Effect on Cloud Cover. Science
- 618 **313**, 655–658 (2006).
- 619 15. Feingold, G., Remer, L.Leach, R. N. and Gibson, C. V.: Assessing the Potential for
- 620 Pyroconvection and Wildfire Blow Ups. A., Ramaprasad, J. & Kaufman, Y. J. Analysis of smoke
- 621 impact on clouds in Brazilian biomass burning regions: An extension of Twomey's approach. J.
- 622 Geophys. Res. 106, 22907-22922 (2001).
- 623 16. Cunningham, C. X., Williamson, G. J. & Bowman, D. M. J. S. Increasing frequency and
- 624 intensity of the most extreme wildfires on Earth. Nat Ecol Evol 8, 1420–1425 (2024).
- 625 17. Ching, J., West, M. & Riemer, N. Quantifying Impacts of Aerosol Mixing State on
- 626 Nucleation-Scavenging of Black Carbon Aerosol Particles. Atmosphere 9, 17 (2018).
- 627 18. J. Operational Meteor., 47–61, https://doi.org/10.15191/nwajom.2021.0904, 2021.
- 628 <u>Li, K., Chen, L., Han, K., Lv, B., Bao, K., Wu, X., Gao, X., and Cen, K.: Smog chamber study</u>
- on aging of combustion soot in isoprene/SO2/NOx system: Changes of mass, size, effective
- density, morphology and mixing state, Atmospheric Research, 184, 139–148,
- 631 https://doi.org/10.1016/j.atmosres.2016.10.011, 2017.

Formatted: Font: Times New Roman

Formatted: Font: Times New Roman, Not Italic

Formatted: Font: Times New Roman

Formatted: Font: Times New Roman, Not Bold

Formatted: Font: Times New Roman

Formatted: Font: Times New Roman, Not Italic

Formatted: Font: Times New Roman

Formatted: Font: Times New Roman, Not Bold

Formatted: Font: Times New Roman

Formatted: Font: Times New Roman
Formatted: Font: Times New Roman

- Loza, C. L., Chhabra, P. S., Yee, L. D., Craven, J. S., Flagan, R. C., and Seinfeld, J. H.:
- 633 <u>Chemical aging of *m*-xylene secondary organic aerosol: laboratory chamber study, Atmospheric</u>
- Chemistry and Physics, 12, 151–167, https://doi.org/10.5194/acp-12-151-2012, 2012.
- Mahfouz, N. G. A. and Donahue, N. M.: Primary ion diffusion charging and particle wall loss in
- smog chamber experiments, Aerosol Science and Technology, 54, 1058–1069,
- 637 https://doi.org/10.1080/02786826.2020.1757032, 2020a.
- Mahfouz, N. G. A. and Donahue, N. M.: Primary ion diffusion charging and particle wall loss in
- smog chamber experiments, Aerosol Science and Technology, 54, 1058–1069,
- 640 https://doi.org/10.1080/02786826.2020.1757032, 2020b.
- Mah, T., McVay, R. C., Pierce, J. R., Seinfeld, J. H., and Ng, N. L.: Constraining uncertainties in
- particle-wall deposition correction during SOA formation in chamber experiments, Atmospheric
- Chemistry and Physics, 17, 2297–2310, https://doi.org/10.5194/acp-17-2297-2017, 2017.
- 644 Ng, N. L., Kroll, J. H., Chan, A. W. H., Chhabra, P. S., Flagan, R. C., and Seinfeld, J. H.:
- Secondary organic aerosol formation from *m*-xylene, toluene, and benzene, Atmospheric
- Chemistry and Physics, 7, 3909–3922, https://doi.org/10.5194/acp-7-3909-2007, 2007.
- Niedermeier, D., Voigtländer, J., Schmalfuß, S., Busch, D., Schumacher, J., Shaw, R. A., and
- Stratmann, F.: Characterization and first results from LACIS-T: a moist-air wind tunnel to study
- aerosol-cloud-turbulence interactions, Atmos. Meas. Tech., 13, 2015–2033,
- 650 https://doi.org/10.5194/amt-13-2015-2020, 2020.
- 651 Reisner, J. M., Josephson, A. J., Gorkowski, K. J., Koo, E., Thompson, D. K., Schroeder, D., and
- 552 <u>Dubey, M. K.: Informed Multi-Scale Approach Applied to the British Columbia Fires of Late</u>
- Summer 2017, JGR Atmospheres, 128, e2022JD037238, https://doi.org/10.1029/2022JD037238,
- 654 <u>2023.</u>
- 655 Riemer, N., West, M., Zaveri, R. A., and Easter, R. C.: Simulating the evolution of soot mixing
- state with a particle-resolved aerosol model, J. Geophys. Res., 114, 2008JD011073,
- https://doi.org/10.1029/2008JD011073, 2009.
- 658 Rodriguez, B., Lareau, N. P., Kingsmill, D. E., and Clements, C. B.: Extreme Pyroconvective
- Updrafts During a Megafire, Geophysical Research Letters, 47, e2020GL089001,
- https://doi.org/10.1029/2020GL089001, 2020.
- Seinfeld, J. H. and Pandis, S. N.: Atmospheric Chemistry and Physics: From Air Pollution to
- Climate Change, 1st ed., John Wiley & Sons, Incorporated, Newark, 1 pp., 2016.
- 663 Shao, Y., Wang, Y., Du, M., Voliotis, A., Alfarra, M. R., O'Meara, S. P., Turner, S. F., and
- McFiggans, G.: Characterisation of the Manchester Aerosol Chamber facility, Atmos. Meas.
- Tech., 15, 539–559, https://doi.org/10.5194/amt-15-539-2022, .

- Taylor, J. W. et al. W., Allan, J. D., Allen, G., Coe, H., Williams, P. I., Flynn, M. J., Le Breton,
- M., Muller, J. B. A., Percival, C. J., Oram, D., Forster, G., Lee, J. D., Rickard, A. R., Parrington,
- M., and Palmer, P. I.; Size-dependent wet removal of black carbon in Canadian biomass burning
- plumes-Atmos. Chem. Phys-14, 13755–13771-(, https://doi.org/10.5194/acp-14-13755-2014)-
- 670 <u>2014.</u>
- 671 19.—The Cloud Collaboration: A study of the link between cosmic rays and clouds with a
- cloud chamber at the CERN PS, https://doi.org/10.48550/ARXIV.PHYSICS/0104048, 2001.
- Wagner, R., Bunz, H., Linke, C., Möhler, O., Naumann, K.-H., Saathoff, H., Schnaiter, M., and
- 674 Schurath, U.: Chamber Simulations of Cloud Chemistry: The AIDA Chamber, in: Environmental
- 575 Simulation Chambers: Application to Atmospheric Chemical Processes, vol. 62, edited by:
- Barnes, I. and Rudzinski, K. J., Kluwer Academic Publishers, Dordrecht, 67–82,
- https://doi.org/10.1007/1-4020-4232-9 5, 2006.
- 678 Wang, J., Doussin, J. F., Perrier, S., Perraudin, E., Katrib, Y., Pangui, E., and Picquet-Varrault,
- 679 B.: Design of a new multi-phase experimental simulation chamber for atmospheric photosmog,
- aerosol and cloud chemistry research, Atmos. Meas. Tech., 4, 2465–2494,
- https://doi.org/10.5194/amt-4-2465-2011, 2011.
- Wang, N., Jorga, S. D., Pierce, J. R., Donahue, N. M., and Pandis, S. N.: Particle wall-loss
- 683 correction methods in smog chamber experiments, Atmos. Meas. Tech., 11, 6577–6588,
- 684 https://doi.org/10.5194/amt-11-6577-2018, 2018.
- Wiedensohler, A., Birmili, W., Nowak, A., Sonntag, A., Weinhold, K., Merkel, M., Wehner, B.,
- Tuch, T., Pfeifer, S., Fiebig, M., Fjäraa, A. M., Asmi, E., Sellegri, K., Depuy, R., Venzac, H.,
- 687 Villani, P., Laj, P., Aalto, P., Ogren, J. A., Swietlicki, E., Williams, P., Roldin, P., Quincey, P.,
- Hüglin, C., Fierz-Schmidhauser, R., Gysel, M., Weingartner, E., Riccobono, F., Santos, S.,
- Grüning, C., Faloon, K., Beddows, D., Harrison, R., Monahan, C., Jennings, S. G., O'Dowd, C.
- D., Marinoni, A., Horn, H.-G., Keck, L., Jiang, J., Scheckman, J., McMurry, P. H., Deng, Z.,
- Zhao, C. S., Moerman, M., Henzing, B., de Leeuw, G., Löschau, G., and Bastian, S.: Mobility
- particle size spectrometers: harmonization of technical standards and data structure to facilitate
- high quality long-term observations of atmospheric particle number size distributions,
- 694 Atmospheric Measurement Techniques, 5, 657–685, https://doi.org/10.5194/amt-5-657-2012,
- 695 <u>2012.</u>
- Yang, F., Hoffmann, F., Shaw, R. A., Ovchinnikov, M., and Vogelmann, A. M.: An
- 697 Intercomparison of Large-Eddy Simulations of a Convection Cloud Chamber Using Haze-
- 698 Capable Bin and Lagrangian Cloud Microphysics Schemes, J Adv Model Earth Syst, 15,
- 699 <u>e2022MS003270</u>, https://doi.org/10.1029/2022MS003270, 2023.
- 700 Yao, Y., Dawson, M. L., Dabdub, D., and Riemer, N.: Evaluating the Impacts of Cloud
- 701 Processing on Resuspended Aerosol Particles After Cloud Evaporation Using a Particle-
- Resolved Model, JGR Atmospheres, 126, e2021JD034992,
- 703 https://doi.org/10.1029/2021JD034992, 2021.

Formatted: Font: Times New Roman

Formatted: Font: Times New Roman

Formatted: Font: Times New Roman, Not Italic

Formatted: Font: Times New Roman

Formatted: Font: Times New Roman, Not Bold

Formatted: Font: Times New Roman

Formatted: Font: Times New Roman

Formatted: Font: Times New Roman

- 704 Yu, H., Gu, H., Sun, Z., Zhou, Y., Chen, J., and Li, Y.: Experimental and Numerical Study on
- the Gravitational Deposition and Coagulation of Aerosols, Front. Energy Res., 10, 840503,
- 706 https://doi.org/10.3389/fenrg.2022.840503, 2022.
- 707 Yu, P., Toon, O. B., Bardeen, C. G., Zhu, Y., Rosenlof, K. H., Portmann, R. W., Thornberry, T.
- 708 D., Gao, R.-S., Davis, S. M., Wolf, E. T., De Gouw, J., Peterson, D. A., Fromm, M. D., and
- Robock, A.: Black carbon lofts wildfire smoke high into the stratosphere to form a persistent
- 710 plume, Science, 365, 587–590, https://doi.org/10.1126/science.aax1748, 2019.
- Zanatta, M. et al., Mertes, S., Jourdan, O., Dupuy, R., Järvinen, E., Schnaiter, M., Eppers, O.,
- 712 Schneider, J., Jurányi, Z., and Herber, A.; Airborne investigation of black carbon interaction with
- low-level, persistent, mixed-phase clouds in the Arctic summer-, Atmos. Chem. Phys-, 23,
- 714 7955–7973-(2023)., https://doi.org/10.5194/acp-23-7955-2023, 2023.
- 715 20. Riemer, N., West, M., Zaveri, R. A. & Easter, R. C. Simulating the evolution of soot mixing
- 716 state with a particle-resolved aerosol model. J. Geophys. Res. 114, 2008JD011073 (2009).
- 717 21. Zaveri, R. A., Barnard, J. C., Easter, R. C., Riemer, N. &., and West, M., Particle-
- 718 resolved simulation of aerosol size, composition, mixing state, and the associated optical and
- cloud condensation nuclei activation properties in an evolving urban plume, J. Geophys. Res,
- 720 115, 2009JD013616-{, https://doi.org/10.1029/2009JD013616, 2010}-,
- 721 22. Ching, J., Riemer, N. & West, M. Black carbon mixing state impacts on cloud
- 722 microphysical properties: Effects of aerosol plume and environmental conditions. JGR
- 723 Atmospheres **121**, 5990–6013 (2016).
- 724 23. Yao, Y., Dawson, M. L., Dabdub, D. & Riemer, N. Evaluating the Impacts of Cloud
- 725 Processing on Resuspended Aerosol Particles After Cloud Evaporation Using a Particle-Resolved
- 726 Model. *JGR Atmospheres* **126**, e2021JD034992 (2021).
- 727 24. Yang, F., Hoffmann, F., Shaw, R. A., Ovchinnikov, M. & Vogelmann, A. M. An
- 728 Intercomparison of Large Eddy Simulations of a Convection Cloud Chamber Using Haze Capable
- 729 Bin and Lagrangian Cloud Microphysics Schemes. J Adv Model Earth Syst **15**, e2022MS003270
- 730 <del>(2023).</del>
- 731 25. Khlystou, A., Kos, G. P. A. & Ten Brink, H. M. A High-Flow Turbulent Cloud Chamber.
- 732 Aerosol Science and Technology 24, 59–68 (1996).
- 733 26. Chang, K. et al. A Laboratory Facility to Study Gas. Aerosol, Cloud Interactions in a
- 734 Turbulent Environment: The IT Chamber. Bulletin of the American Meteorological Society 97,
- 735 <del>2343–2358 (2016).</del>
- 736 27. Niedermeier, D. et al. Characterization and first results from LACIS-T: a moist-air wind
- 737 tunnel to study aerosol-cloud-turbulence interactions. Atmos. Meas. Tech. 13, 2015-2033
- 738 <del>(2020).</del>

Formatted: Font: Times New Roman

Formatted: Font: Times New Roman

Formatted: Font: Times New Roman, Not Italic

Formatted: Font: Times New Roman

Formatted: Font: Times New Roman, Not Bold

Formatted: Font: Times New Roman

Formatted: Font: Times New Roman, Not Italic

Formatted: Font: Times New Roman

Formatted: Font: Times New Roman, Not Bold

Formatted: Font: Times New Roman

Formatted: Font: Times New Roman

Formatted: Font: Times New Roman

- 739 28. Shao, Y. et al. Characterisation of the Manchester Aerosol Chamber facility. Atmos.
- 740 Meas. Tech. 15, 539-559 (2022).
- 741 29. The Cloud Collaboration. A study of the link between cosmic rays and clouds with a
- 742 cloud chamber at the CERN PS. Preprint at https://doi.org/10.48550/ARXIV.PHYSICS/0104048
- 743 <del>(2001).</del>
- 744 30. Wagner, R. et al. Chamber Simulations of Cloud Chemistry: The AIDA Chamber. in
- 745 Environmental Simulation Chambers: Application to Atmospheric Chemical Processes (eds.
- 746 Barnes, I. & Rudzinski, K. J.) vol. 62 67–82 (Kluwer Academic Publishers, Dordrecht, 2006).
- 747 31. Corner, J. & Pendlebury, E. D. The Coagulation and Deposition of a Stirred Aerosol. *Proc.*
- 748 Phys. Soc. B **64**, 645–654 (1951).
- 749 32. Fotou, G. P. & Pratsinis, S. E. A Correlation for Particle Wall Losses by Diffusion in Dilution
- 750 Chambers. Aerosol Science and Technology 18, 213–218 (1993).
- 751 33. Wang, N., Jorga, S. D., Pierce, J. R., Donahue, N. M. & Pandis, S. N. Particle wall loss
- 752 correction methods in smog chamber experiments. Atmos. Meas. Tech. 11, 6577-6588 (2018).
- 753 34. Mahfouz, N. G. A. & Donahue, N. M. Primary ion diffusion charging and particle wall loss
- 754 in smog chamber experiments. Aerosol Science and Technology 54, 1058–1069 (2020).
- 755 35. Crump, J. G. & Seinfeld, J. H. Turbulent deposition and gravitational sedimentation of an
- 756 aerosol in a vessel of arbitrary shape. Journal of Aerosol Science 12, 405–415 (1981).
- 757 <del>36. Crump, J. G., Flagan, R. C. & Seinfeld, J. H. Particle Wall Loss Rates in Vessels. *Aerosol*</del>
- 758 Science and Technology **2**, 303–309 (1982).
- 759 37. Particula [computer software]. uncscode/particula: v0.1.3. Zenodo
- 760 https://doi.org/10.5281/ZENODO.6634653 (2025).
- 761 38. Seinfeld, J. H. & Pandis, S. N. Atmospheric Chemistry and Physics: From Air Pollution to
- 762 Climate Change. (John Wiley & Sons, Incorporated, Newark, 2016).
- 763 39.—Zong, T. et al., Wu, Z., Wang, J., Bi, K., Fang, W., Yang, Y., Yu, X., Bao, Z., Meng, X.,
- Zhang, Y., Guo, S., Chen, Y., Liu, C., Zhang, Y., Li, S.-M., and Hu, M.; A new smog chamber
- 765 system for atmospheric multiphase chemistry study: design and characterization. Atmos. Meas.
- 766 Tech-...16, 3679–3692-<u>1, https://doi.org/10.5194/amt-16-3679-2023, 2</u>023<del>).</del>
- 767 40. Wang, J. et al. Design of a new multi phase experimental simulation chamber for
- 768 atmospheric photosmog, aerosol and cloud chemistry research. Atmos. Meas. Tech. 4, 2465–
- 769 <del>2494 (2011).</del>

Formatted: Font: Times New Roman

Formatted: Font: Times New Roman

Formatted: Font: Times New Roman, Not Italic

Formatted: Font: Times New Roman

Formatted: Font: Times New Roman, Not Bold

Formatted: Font: Times New Roman

Formatted: Font: Times New Roman

1	system: Changes of mass, size, effective density, morphology and mixing state. <i>Atmospheric</i>
2	Research 184, 139–148 (2017).
3	42. Hussein, T. et al. Deposition rates on smooth surfaces and coagulation of aerosol
4	particles inside a test chamber. Atmospheric Environment 43, 905–914 (2009).
7	particles inside a test chamber. Atmospheric Environment 48, 505–514 (2005).
5	43. Yu, H. et al. Experimental and Numerical Study on the Gravitational Deposition and
6	Coagulation of Acrosols. Front. Energy Res. 10, 840503 (2022).

Li, K. et al. Smog chamber study on aging of combustion soot in isoprene/SO2/NOx